Structural, Optical and Electrical Properties of $CaSnO_3$ and $Ca_{0.98}Nd_{0.02}Sn_{0.98}Ti_{0.02}O_3$ Synthesized using Sol-Gel Method

Aditya Kumar[1], **Bushra Khan**[1], **Gulab Singh**[1], **Manoj K. Singh**[1,*], **Upendra Kumar**[2,*]

[1]Centre of Material Sciences, University of Allahabad, Prayagraj 211002, India
[2]Department of Physics, Banasthali Vidyapith, Banasthali 304022, India

***Corresponding authors: E-mail: mksingh100@yahoo.com (Manoj K Singh); upendra.bhu512@gmail.com (Upendra Kumar)**

DOI: 10.5185/amlett.2021.031611

Single phase sample of $CaSnO_3$ and $Ca_{0.98}Nd_{0.02}Sn_{0.98}Ti_{0.02}O_3$ were synthesized by sol-gel route followed by calcination at 800°C. The X-ray diffraction pattern of both samples showed monophasic, and their Rietveld refinement studies indicated that the samples belonged to orthorhombic crystal structure under space group *Pbnm*. Moreover, dopant substitution results in unit cell compression due to lower ionic radii of dopant than host. UV-Vis. spectroscopy study of samples reflected semiconducting samples. The direct optical band gap of doped sample found smaller (4.02 eV) than undoped (4.23 eV), due to formation of Nd^{3+} state below conduction band. The dielectric constant of both samples (30 and 18) was found to be temperature independent up to 220°C and 300°C and tangent loss below 1 makes it suitable candidate for thermally stable capacitor application. Ac conductivity of samples was analyzed using Arrhenius model as a function of frequency and temperature, and the value of activation energy is reflected an electronic as well as mixed ionic and electronic conduction in samples. Based on these studies, the present material can be used in UV-filter, sensors, and mixed ionic and electronic conductor applications.

Introduction

The $MSnO_3$ (M: Alkaline earth metal) materials belong to perovskite class, firstly studied by Russian mineralogist Lev Perovski [**1**]. Based on the valence states of different alkaline earth metal different kinds of structures are possible [**2-5**]. Modifying hetrovalent and homovalent doping at either M-site, Sn-site or both site simultaneously exhibiting versatile properties such as, optical, electrical and electronic properties [**3-8**]. Calcium stannate was placed at the top of the alkaline earth stannate group and had a spectacular property over the other stannates, including display device applications, thermally stable capacitors, gas sensors and actuator applications [**9-12**]. The homovalent doping on Ca and Sn-site of $CaSnO_3$ provides structural stabilization, while hetrovalent doping enhances the oxygen stoichiometry, that tunes the concentration of Sn^{4+}/Sn^{2+} which has been played a crucial role in optical memory storage, lithium ion battery and host matrix for phosphor applications [**13-15**]. Due to higher value of dielectric constant of $CaSnO_3$, it has been further used in random access memory application. On the other hand, the $CaSnO_3$ displays a wide optical band gap (4.3 eV), that grab sufficient interest to use it as a n-type semiconductor [**16,17**].

Different types of synthesis techniques such as solid state reaction (SSR), hydrothermal method, method of co-precipitation, sol – gel, solvo-thermal method, and auto combustion method etc. were used to produce advance materials [**11,12,18-20**]. These synthesis techniques are important, but also have certain limitations. In case of the solid-state reaction technique, the materials can react without any chemical solvents by inter surface diffusion and yield highly pure materials. The method's main drawback is that it required high temperature for solid inter-diffusion [**21,22**]. For hydrothermal technique, however, the raw materials were taken in form of hydroxide and requiring high pressure to tune chemical reaction and surface morphology. The higher cost of autoclaves makes this method impractical for bulk production of materials [**23**]. For co-precipitation technique, acetate form of raw materials was taken and their oxides precipitated, then these obtained powders reacted at relatively lower temperatures than other above discussed method. The lower reaction temperature for co-precipitation method is the great advantage over other method, but the major disadvantage of this method is the chemical loss during precipitation of materials resulting in lower yields relative to other methods [**24**]. These all synthesis techniques used to process advance materials have a number of advantage and disadvantages. Among these all investigated preparatory methods, the sol-gel technique is of enormous importance because of its low cost, low temperature, high yield, high phase purity and eco-friendly nature of reaction, which makes this method very important for the development of advanced nanomaterials [**25-28**].

It is a well-known fact that physical and chemical properties of perovskite dependent on the surface morphology, particle size, and processing parameters

[**25,29**]. There are now numerous efforts made to prepare pure and doped $CaSnO_3$ via various synthesis routes adopted by scientist and his co-workers. M. Tsega and his team successfully synthesized Eu doped $CaSnO_3$ using sol-gel method and studied their optical band gap and luminescence properties at room temperature and found it as a wide band gap semiconductor that possess intense emission in orange region [**30**]. Synthesis of $CaSnO_3$ using hydrothermal process at 500℃ reported by H. Cheng and Z. Lu and reported its gas sensing behaviour in terms of its sensitivity [**16**]. Iron (Fe) and cobalt (Co) doped Calcium stannate was synthesized using sol-gel method and investigate their structural and optical behaviours by S. Sumithra and N. Victor Jaya [**31,32**]. With transition metal doping in calcium stannate, the optical band gap of samples was tuned approx. ~ 1 eV. Because of this tuning behaviour, these materials exhibit great impact on pure and doped $CaSnO_3$ for optoelectronic and spintronics device applications [**31-33**]. A. M. Azad and team reported the electrical properties (impedance, Capacitance, modulus etc.) of $CaSnO_3$ as a function of temperature and frequency [**9,10**].

Jules Goethals *et. al.*, stated that, with incorporation of Nd at Ca-site below 28 wt.%, it crystallized into orthorhombic structure under *Pbnm* space group, while the structure becomes rock salt under space group $P2_1/n$ above 28 wt.% [**34**]. However, only luminescence properties were reported for Nd modified $CaSnO_3$. S. Singh *et. al.*, reported that Ti-substitution in $CaSnO_3$ improved dielectric and electrical properties and it could be used as an oxygen ion conductor within the investigated temperature range [**35**].

Therefore, based on the report by Jules Goethals *et. al.*, and S. Singh *et. al.*, it has been noticed that combining Nd at Ca-site and Ti at Sn site would serve as a candidate for thermally stable capacitor and oxygen ion conductor within investigated temperature range [**34,36**]. According to Hume-Rothery criteria, the ionic difference between the Nd^{3+} and Ca^{2+} as well as Ti^{4+} and Sn^{4+} was found to be ±15%, which makes it suitable Nd^{3+} and Ti^{4+} as dopant for Ca^{2+} and Sn^{4+} site respectively [**37**]. To the best of author's knowledge, no report is available on simultaneous substitution of Nd^{3+} at Ca-site and Ti^{4+} at Sn-site of $CaSnO_3$ and their impact on structural, optical and electrical properties. Such kinds of research are important not only for the development of new materials, but also for the basic understanding of solid-state physics involved in the study.

Therefore, to fulfil the aim of this work, the pure and simultaneous Nd and Ti-doped $CaSnO_3$ samples were synthesized using Sol-Gel chemical route followed by two step heat treatment. Preliminary and phase confirmation of samples was investigated using X-ray diffraction and Rietveld refinement study. Optical properties of samples were studied using UV-Vis. spectroscopy. The electrical properties of sintered samples were studied in temperature range 25 to 500ºC at three different frequencies 1 KHz, 10 KHz and 100 KHz.

Experimental methods

Materials

We purchased all the chemicals from Alfa Aesar for the synthesis of $CaSnO_3$ (CSONT 0) and $Ca_{0.98}Nd_{0.02}Sn_{0.98}Ti_{0.02}O_3$ (CSONT 2) samples. Here, calcium nitrate tetra hydrate ($Ca(NO_3)_2.4H_2O$, purity 98%), neodymium nitrate ($Nd(NO_3)_2.xH_2O$, purity 98%), tin (iv) chloride hydrate ($SnCl_4.xH_2O$, purity 98%) and tetrabutyl titanate ($C_{16}H_{36}O_4Ti$, purity 98%) were used as source materials of Ca^{2+}, Nd^{2+}, $Sn^{4+}$and Ti^{4+} respectively. Deionized (DI) water, Citric acid ($C_6H_8O_7$), and polyvinyl alcohol (PVA) were used as solvent, catalyst and binder respectively for these materials. Complete raw chemicals are analytical reagents used without further purging.

Synthesis of CSONT 0 and CSONT 2 samples

Analytical grade calcium nitrate tetra hydrate and tin (iv) chloride hydrate were used as raw materials to synthesize $Ca_{1-x}Nd_xSn_{1-y}Ti_yO_3$ (x = 0.00 and 0.02, y = 0.00 and 0.02) samples. Initially, the $Ca(NO_3)_2.4H_2O$ and $Nd(NO_3)_2.xH_2O$ was taken in stoichiometric ratio 0.98:0.02 and dissolved separately in 50 ml DI water. Similarly, the aqueous solution of $SnCl_4.xH_2O$ and $C_{16}H_{36}O_4Ti$ were prepared in same stoichiometric ratio. Then all these solutions were transferred into a large beaker and placed on a hot plate with constant stirring till formation of clear homogeneous solution. Thereafter, citric acid (CA) was added to solution in molar ratio1:6 to $SnCl_4.xH_2O$. Now, the solution was heated slowly up-to 80°C with constant stirring for 12 hours with magnetic stirrer till the formation of transparent solution. Now, NaOH was added to this solution dropwise till precipitation keeping the pH of solution 9-10. Since the basic medium of solution favours, the precipitation. This process continued until the gel formation. The obtained gel was further heated at 120ºC on the magnetic hot plate for 24 h, until the ignition started. Once the ignition started, it was burned completely and formed a black powder. Now, the obtained powder was transferred to alumina crucible and placed in muffle furnace and calcined at 800℃ for 12 h. The calcined powder was blended with polyvinyl alcohol (PVA) 10 wt.% for the preparation of pellets. Subsequently, the obtained powder was pressed into disc shape (10mm diameter and 1mm thickness) pellets using hydraulic press by applying the pressure of 7 kN. After that, the pellets were fired at 900°C for 16 hours in ambient air using a programmable heat furnace. Finally, these sintered pellets coated with conductive silver paste on both surfaces and dried at 100°C for 2 hours to remove moisture and hydrocarbons of binder (PVA). The obtained powders and pellets were then projected for various characterization techniques. The schematic diagram of several steps involved in synthesis process was shown in **Fig. 1**.

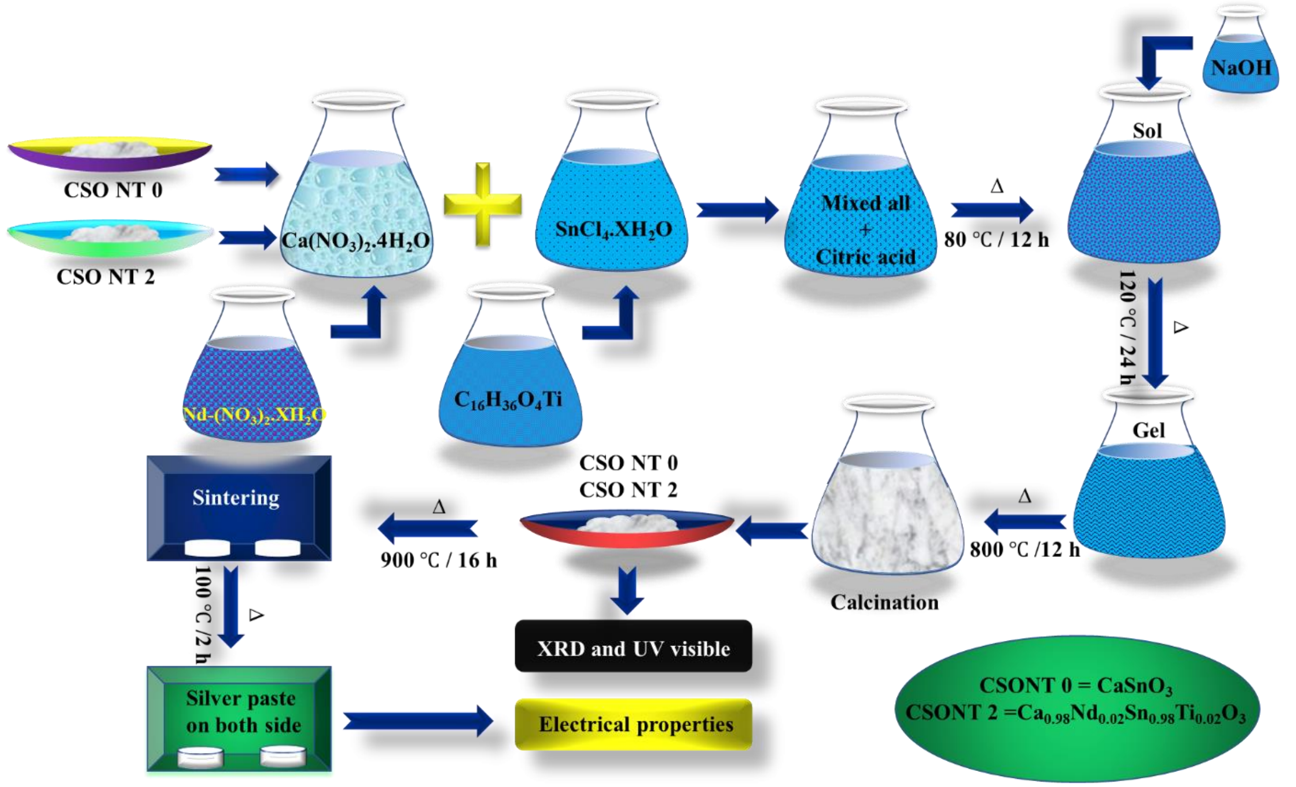

Fig. 1. Schematic diagram of the steps involved in synthesis of CSONT 0 and CSONT 2.

Characterization

X-ray diffraction

The X-ray diffraction pattern of CSONT 0 and CSONT 2 samples were characterised by using Bruker D8 advance (U.S.A) with Cu-Kα radiation of wavelength 0.15406 nm. X-ray diffraction pattern were recorded in $20 \leq 2\theta \leq 80$ with step size 0.05° at room temperature. Recorded data was further examined by Rietveld refinement taking help FullProf software suite.

Uv-Vis. analysis

The room temperature Uv-Vis reflection spectra of synthesised samples were recorded between the 200-800 nm wavelengths by using Cary-4000 UV-Vis. spectrophotometer. Additionally, band gaps of samples were calculated by Kubelka Munk function.

Electrical measurements

Electrical measurement of all synthesised samples such as dielectric constant, tangent loss and ac conductivity were recorded by using Alfa-A High-Frequency Impedance Analyzer novo-control Technologies.

Results and discussions

Phase analysis using Powder X-ray diffraction

Phase formation and crystal structure of samples were performed using XRD technique. **Fig. 2** depicts the powder XRD pattern of samples. All diffraction patterns are fine, specifying perfect crystalline nature of sample. The theoretical JCPDS database (file no JCPDS 77-1797) belongs to the orthorhombic crystal structure was perfectly matched with the XRD pattern [**38**]. For sample CSONT 0, the most intense peak observed for plane (112) at angular position 32.05° was shifted towards higher angle at 32.1° for sample CSONT 2. The shift in position of most intense peak to higher angle may be related to the lower ionic radii of Nd^{3+} (1.27 Å) than Ca^{2+} (1.34 Å) and Ti^{4+} (0.605 Å) than Sn^{4+} (0.69 Å) [**39**]. According to Bragg's law, the lattice constant is inversely proportional to the sine of Bragg angle $a \propto 1/\mathrm{Sin}\,\theta$, so that the resulting lattice constant should be lower if the lower ionic radius replaced to host atom. Lower value of lattice constant reflects higher Bragg angle, and this assumption supports our experimental result.

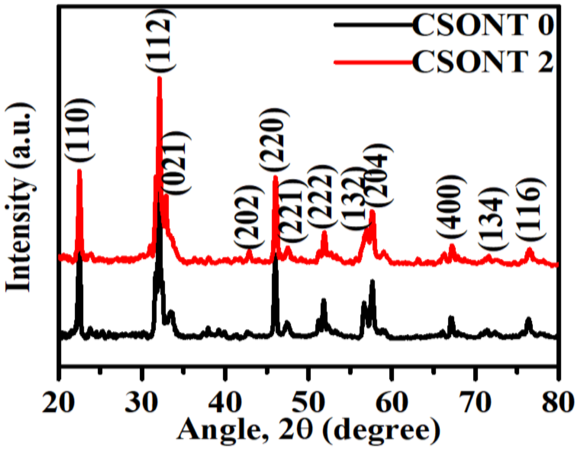

Fig. 2. Room temperature XRD pattern of as prepared samples.

Table 1. Rietveld refinement parameters, lattice parameters, volume, XRD density of samples.

Parameters	CSONT0	CSONT2
a (Å)	5.5109	5.5105
b (Å)	5.6485	5.6417
c (Å)	7.8747	7.8742
V ($Å^3$)	245.12	244.80
ρ (gm/cm^3)	5.1	5.15
R_p	7.2	8.4
R_{wp}	7.6	9.2
R_e	7.0	9.0
$S=R_{wp}/R_p$	1.05	1.09
χ^2	4.25	5.12

Furthermore, to determine the structural parameters more accurately, the XRD pattern was analyzed by Rietveld refinement using FullProf software suite. In order to perform refinement, the crystal structure was taken as orthorhombic with space group $Pbnm$. The background points for XRD pattern were defined in terms of sixth order polynomial coefficient. All parameters such as lattice parameters, peak profile parameters (u, v, w, η_0, I_g, x), atomic co-ordinates (x, y, z, B, and Occupancy) varied during refinement until perfect match between generated and experimental XRD pattern. The goodness of fitting was measured from calculating the parameters $(S)=R_{wp}/R_e$ and provided in **Table 1**. It was noted from Table 1 that the value of S found close to unity and reflects accuracy of derived parameters [40]. Rietveld refinement pattern of samples were shown in **Fig. 3**. Value of the lattice parameters, volume of unit cell, and the X-ray density were obtained from refinement, and indexed in **Table 1**. For samples CSONT 2, unit cell parameters and volume were found to be lower than CSONT 0, which could be attributed to lower ionic radii of Nd^{3+} (1.27 Å) in comparison to Ca^{2+} (1.34 Å) and Ti^{4+} (0.605 Å) than Sn^{4+} (0.69 Å). The X-ray density of the doped sample, however was higher than undoped due to heavier atomic masses of Nd and Ti, and slight lower unit cell volume.

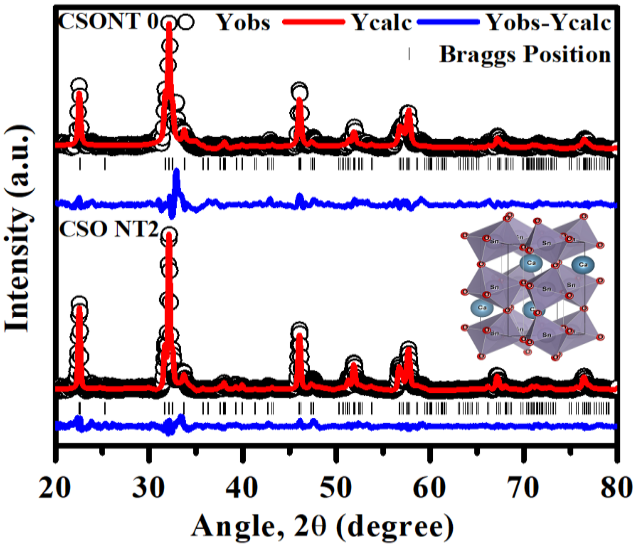

Fig. 3. Rietveld refinement XRD pattern of sample under crystal structure orthorhombic and space group $Pbnm$.

Determination of crystallite size

The broadening of XRD peak is associated with smaller crystalline size and contribution of micro-strain. The crystallite size of the samples was determined mathematically by formula [**41**];

$$D = \frac{0.9\lambda}{\beta Cos\theta} \tag{1}$$

where, λ is wavelength of Cu Kα radiation, β is full width at half maxima (FWHM), and θ is angular position of Bragg diffraction peak. Crystallite size for samples was calculated using FWHM of all diffraction peaks and calculated value of crystallite site for each peak using Eq. (1) are given in **Table 2**. From Table 2, it showed lower crystallite size for CSONT 2 than CSONT 0 sample. Since the peak broadening also had contribution of micro-strain, therefore the value of crystallite size was not correct in this case. To determine the accurate value of crystallite size, separating the micro-strain value from the XRD peak is essential. A well-known relation was used to assess the micro-strain present in sample known as Williamson-Hall (W-H) plot described in literature [42]. According to this plot, the total width of XRD peak can be written as the sum of contribution arised due to smaller crystallite size (β_D) and micro-strain (β_ϵ).

$$\beta = \beta_D + \beta_\epsilon \tag{2}$$

The value of β_D from Debye Scherrer equation and β_ϵ as $4\epsilon \tan\theta$ was put in equation (2) and found to be [43];

$$\beta = \frac{0.9\lambda}{DCos\theta} + 4\epsilon \tan\theta \tag{3}$$

$$\beta Cos\theta = \frac{0.9\lambda}{D} + 4\epsilon \operatorname{Sin}\theta \tag{4}$$

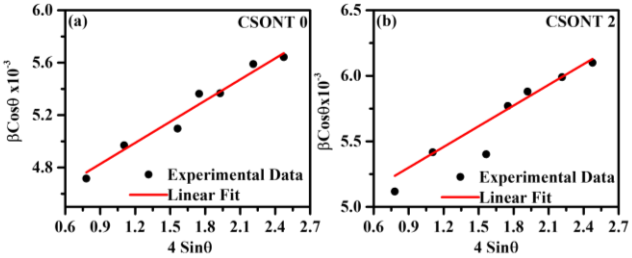

Fig. 4 Williamson-Hall plot generated from XRD data using equation (4).

W-H plot for samples CSONT 0 and CSONT 2 were generated using equation (4) and shown in **Fig. 4**. The linear relationship found between $\beta Cos\theta$, and $4 \operatorname{Sin}\theta$, implies that the straight line has slope ϵ and its intercept on y-axis is $\frac{0.9\lambda}{D}$. The intercept and slope value were used to determine crystallite size and micro-strain respectively, and given in **Table 2**. Table 2 showed that the crystallite size follows the same trend as that obtained from the Debye Scherrer equation. Nevertheless, the value obtained from the W-H plot is higher than that obtained from Debye Scherer equation. Equation (1) and (4) indicate that crystallite size is inversely proportional to the FWHM of XRD peak. Due to contribution of micro-strain within FWHM of XRD peak, the FWHM after exclusion of micro-strain is lower than the total FWHM of XRD peak.

Table 2. Crystallite size and micro-strain obtained from Debye Scherrer, W-H plot and SSP plot.

S. No	Position of peak		FWHM of peak		Debye Scherrer Crystallite size (nm)		W-H plot			
							CSONT0		CSONT2	
	CSONT0	CSONT2	CSONT0	CSONT2	CSONT0	CSONT2	Size	Strain	Size	Strain
1	22.49491	22.5201	0.27552	0.29896	30.72	28.31	31.94	$3.34x10^{-3}$	28.70	$4.68x10^{-3}$
2	32.07081	32.11641	0.44106	0.97483	19.58	8.86	SSP plot			
3	45.99986	46.04791	0.31729	0.33627	28.42	26.82	Size	Strain	Size	Strain
4	51.81756	51.89084	0.36635	0.42663	25.19	21.64	35.82	$3.64x10^{-3}$	30.26	$4.84x10^{-3}$
5	57.62122	57.34409	0.47533	1.37795	19.93	6.87				
6	67.14018	67.23545	0.3322	0.34377	29.99	28.99				
7.	76.37813	76.49274	0.44007	0.47733	23.99	22.14				
Average Crystallite size					25.40	20.52				

Therefore, the value of crystallite size after micro-strain correction is higher. The micro-strain of doped sample is observed to be greater than undoped, which may be due to difference in the ionic radii of Nd^{3+} and Ti^{4+} compared to host ion.

Since, in the case of W-H plot, XRD peaks are considered as Lorentzian due to isotropic nature of line broadening. However, in Lorentzian function, the reflection obtained from the lower angle gets more weightage. The error function has higher value at lower angle. Therefore, due to isotropic line broadening, a fantastic evaluation of the crystallite size and strain present in samples can be determined using a well-known relation formerly known as "Size–Strain plot" (SSP). In the Size–Strain plot" (SSP) plot, the crystallite size of the samples is modeled by Lorentzian function, while strain by Gaussian functions, and given as [**44**].

$$\left(\frac{d\beta Cos\theta}{\lambda}\right)^2 = \frac{k\lambda}{D}\left(\frac{d^2\beta Cos\theta}{\lambda^2}\right) + \left(\frac{\varepsilon}{2}\right)^2 \qquad (5)$$

where, d is the interplanar spacing while ε represented average strain in sample. Other parameters are already described in equation (3) and (4). The SSP plot of samples CSONT 0 and CSONT 2 were successfully generated using Eq. (5) and shown in **Fig. 5**. The linear equation was fitted to the experimental data describing the slope as $\frac{k\lambda}{D}$, and intercept to $\left(\frac{\varepsilon}{2}\right)^2$. The crystallite size of sample was calculated using the slope of straight line, while square root of intercept was used to evaluate the value of strain. The average value of crystallite size and micro-strain obtained by SSP plot was given in **Table 2**, follows similar trends as seen from Debye Scherrer equation. On carefully observation, the value obtained from SSP plot is higher than the value obtained from Debye Scherrer equation. However, micro-strain value for doped sample was again found higher for doped sample than undoped, due to lower ionic radii of dopant. As lower ionic radii occupied the specified host atom site, the crystal structure becomes unstable, which can give a kind of structural transition although no structural transition was observed from the refinement studies of XRD data. Thus, lattice strain values increase to stabilize the crystal structure.

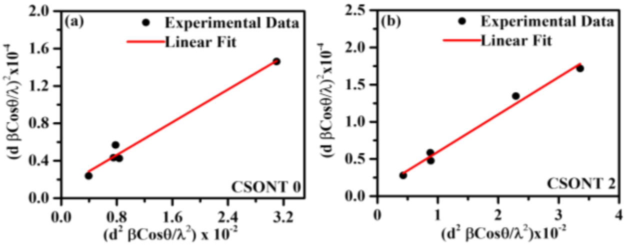

Fig. 5. Size-strain plot generated from XRD data using equation (5).

Study of reflectance spectra and optical band gap

Using UV-Vis spectroscopy, the optical properties of samples were recorded in reflectance mode. **Fig. 6(a)** shows the experimental reflectance spectra, showing minimum reflectance in UV-Vis and maximum in visible-near infrared region for undoped sample, while doped sample shows several reflectance peaks within the investigated wavelength range. The several peaks observed within 200-800 nm were assigned with number from (1) to (10), describing transitions from intermediate states of Nd^{3+}. These transitions were occurred from Nd^{3+}:$4I_{9/2}$ level to excited states ($2P_{1/2}$, $2D_{15/2}$), ($4G_{11/2}$, $4G_{9/2}$, $2D_{2/3}$, $2K_{15/2}$), ($2K_{13/2}$, $4G_{7/2}$, $4G_{9/2}$), ($4G_{5/2}$, $2G_{7/2}$), $4F_{9/2}$, ($4F_{7/2}$, $4S_{3/2}$), ($4F_{5/2}$, $2H_{9/2}$), $4F_{3/2}$ [**7,45**]. Therefore, based on these reflectance states, materials find application in UV radiation filters, sensors and imaging application. The reflectance spectra were analyzed using Kubelka-Munk theory to determine the maximum absorbance of sample that could occur in the UV-region. According to Kubelka-Munk theory, the Kubelka-Munk function was determined mathematically using the value of reflectance by formula [**46**];

$$F(R) = \frac{1-R^2}{2R} \qquad (6)$$

Kubelka-Munk function F(R) value determined using equation (6) was plotted in **Fig. 6(b)**. The onset absorbance of sample was determined by extrapolating linear region to the wavelength axis. The optical absorption edges were 295.71 nm and 334.86 nm for samples CSONT 0 and CSONT 2 respectively. The increased absorbance edge for Nd-Ti doped sample reflected a red shift in the sample due to the formation of Nd^{3+} intermediate states below the conduction band. The band gap of samples was calculated from the Kubelka-

Munk function F(R) by plotting the square of F(R)*(hν) versus hν, as shown in **Fig. 6(c)**. The linear portion of the curve extrapolated on X-axis gives the corresponding value of direct optical band gap. Band gap of the sample obtained from direct transition was indexed in **Fig. 6(c)**, which was found to be smaller for CSONT 2 (4.02 eV) than CSONT 0 (4.23 eV). As we found several weak intensity reflectance peaks (due to defect) in reflectance spectra, the sample can also exhibit an indirect band gap. Accordingly, the optical band gap for the indirect allowed transitions was determined by plotting the square route of the product F(R) with energy (hν) versus hν as shown in **Fig. 6(d)**. The indirect band gap of samples was determined using similar procedure such as extrapolating the linear region of curve to X-axis. The indirect band gap for CSONT 2 sample was 3.16 eV lower than sample CSONT 0 i.e., 3.69 eV. The value of direct and indirect bandgap showing an inorganic semiconducting nature of samples. The difference in the value of direct band gap for both samples was found to be 0.21 eV, while 0.53 eV for indirect band gap. It reflects that the separation between the fermi level to conduction band decreases with incorporation of Nd-Ti, that may be due to creation of a Nd absorbance state which favours transition from these states. The difference in direct band gap and indirect band gap of same samples was found to be 0.54 eV and 0.86 eV for sample CSONT 0 and CSONT 2 respectively, suggesting presence of defects in samples [**47**]. Since the samples were synthesized at high temperature, so the presence of oxygen vacancies can't be ruled out. The presence of oxygen vacancy can be understood as follows;

$$O_o \rightarrow \frac{1}{2} O_2(g) + V_o^{\cdot\cdot} + 2e' \quad (7)$$

In ceramics, the most common defects found in the samples are, $V_O^x, V_{\dot{O}}$, and $V_{\ddot{O}}$, as the difference in the value of direct and indirect band gap is nearly equal, indicating similar type defects in the sample. The difference value found slight higher for CSONT 2 than CSONT0 that might be due to difference in concentration of oxygen vacancies in both samples [**41**].

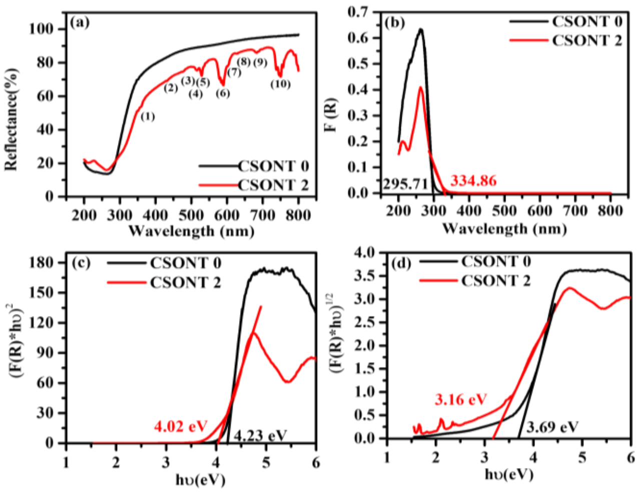

Fig. 6. (a) Room temperature reflectance spectra (b) Kubelka-Munk Function (c) Plot of $(F(R) * h\nu)^2$ vs. $h\nu$ (d) plot of $(F(R) * h\nu)^{1/2}$ vs. $h\nu$ for the samples.

By utilizing these states as metastable states, the present material can be explored for various semiconductor device applications.

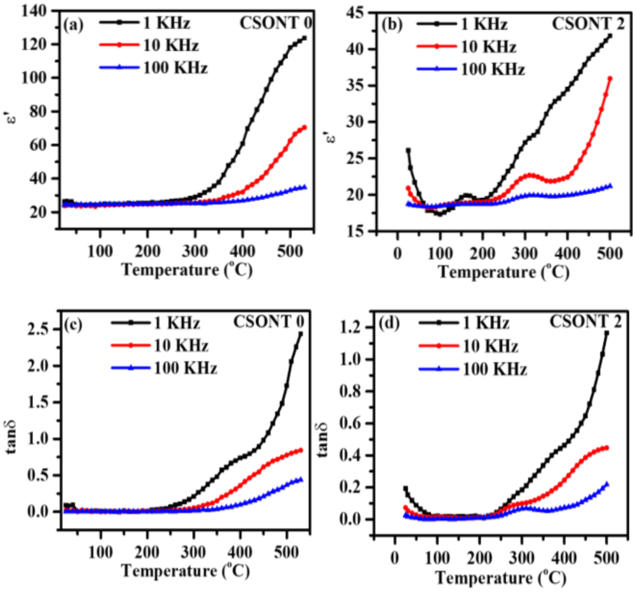

Fig. 7. Temperature dependent dielectric constant at different frequency of **(a)** CSONT 0 **(b)** CSONT 2, Temperature dependent tangent loss at different frequency of **(c)** CSONT 0 **(d)** CSONT 2.

Study of dielectric, tangent loss and AC-conductivity

The dielectric properties of sintered samples were analyzed as a function of frequency and temperature. **Fig. 7(a)** and **Fig. 7(b)** depict the variation in real part of dielectric constant with temperature at three different frequencies: 1 KHz, 10 KHz, and 100 KHz for samples CSONT 0 and CSONT 2. The value of ε for sample CSONT0 is found to be independent of temperature up to 280°C and subsequently increased linearly with temperature up to 530°C, suggesting temperature dependent polarization in sample. Nevertheless, the dielectric constant decreases with increasing frequency. Furthermore, for sample CSONT 2, the value of ε is almost independent of temperature up to 200°C at 10 KHz and 100 KHz, while the temperature-dependent dielectric constant includes a transition peak at 150°C for 1 KHz, 295°C for 10 KHz and 310°C for 100 KHz, which again indicates temperature-dependent polarization in sample CSONT 2. Since the overall electrical properties of ceramics is resulted due to contribution of various types polarizations such as electronic polarization, dipolar polarization, interfacial polarization, and ionic polarization [**48-50**]. These polarizations can be interpreted as follows;

Interfacial polarization is caused by local microheterogeneity, which has two different conductivity values and results in a very high value of dielectric constant. Typically, this form of polarization occurred from 1 mHz to 1 KHz.

Orientational polarization occurs due to dipole orientation (the same kind of charge with the opposite in nature placed apart formed a dipole) in the presence of small ac electric field. This form of polarization was found to be active in frequency range from 1 KHz to 1 MHz.

Ionic polarization is the process of ionization of atoms (separation of charge to ionize the atom) in the presence of electric field. This form of polarization found to be active from 1 MHz to 1 GHz.

Finally, electronic polarization results from electron motion in the presence of ac electric field. This polarization occurs at frequencies above 1 GHz.

Therefore, in the present study, based on available frequency, only two kinds of polarization were expected in present sample, such as interfacial polarization and orientational polarization. In this case, the sample CSONT 0 was synthesized at high temperature therefore, the loss of oxygen can't be ruled out and formation of oxygen vacancy in sample given by equation (7). Nonetheless, the presence of electron in equation (7) reduced Sn^{4+} in Sn^{2+} by following equation;

$$Sn^{4+} + 2e' \rightarrow Sn^{2+} \tag{8}$$

The presences of Sn^{2+} at Sn^{4+} acts as a negative defect and denoted by $Sn^{2+}{}_{Sn^{4+}}''$ which located apart with oxygen vacancy $V_o^{\cdot\cdot}$ and formed a dipole (equal magnitude of charge placed at finite distance) that responded in the presence of an electric field by hopping of electron in terms of dipole orientation.

In case of doped sample CSONT 2, the dielectric constant was found to be lower, either due to a reduction in the number of dipoles or a greater distance between dipoles. Since the substitution of Nd at Ca acts as hetrovalent while Ti at Sn^{4+} acts as homovalent and the charge compensation mechanism will take place as follow;

$$Nd_2O_3 + 2TiO_2 \xrightarrow{2CasnO_3} 2Nd_{Ca}^{\cdot} + 2Ti_{Sn}^{x} + \frac{2e'}{V_{Ca}''} + 10O_O^x + \frac{1}{2}O_2 + V_{\ddot{O}} + 2e' \tag{9}$$

Presence of electron further reduced the valence state of Ti^{4+} as

$$Ti^{4+} + e' \rightarrow Ti^{3+} \tag{10}$$

$$Ti^{3+} + e' \rightarrow Ti^{2+} \tag{11}$$

Since the higher number of electrons due to the substitution of Nd, the number of dipole increases, such as $Sn^{2+}{}_{Sn^{4+}}'' - V_o^{\cdot\cdot}$, $Ti^{2+}{}_{Ti^{4+}}'' - V_o^{\cdot\cdot}$ and therefore the dielectric constant should be increased. However, the experimental finding shows opposite to the expectation. The decrease in dielectric constant could be due to the following reasons;

(i) The charge compensation mechanism takes place by creating vacancy of Ca (V_{Ca}'') and the dipoles are formed between $V_{Ca}'' - V_{\ddot{O}}$ which is heavier than dipoles $Sn^{2+}{}_{Sn^{4+}}'' - V_o^{\cdot\cdot}$, and $Ti^{2+}{}_{Ti^{4+}}'' - V_o^{\cdot\cdot}$ and does not respond in presence of an ac field. This decreases the net dielectric constant for doped sample.

(ii) If the charge compensation mechanism occurs by creation of electron, then the sample contains a large number of electrons resulting increased the conduction of electron, and dielectric properties and conduction are directly opposite to each other.

Moreover, the transition peak observed in dielectric curve was due to hopping of electron between degenerate sites of Sn^{4+}/Sn^{2+} or $Ti^{4+}/Ti^{3+}/Ti^{2+}$ [**51,52**].

Fig. 7(c) and **Fig. 7(d)** illustrate the variation of tanδ with temperature at three different frequencies: 1 KHz, 10 KHz, and 100 KHz. Initially, the tangent loss for sample CSONT 0 is found to be independent of temperature up to 250°C, and then increased with temperature. Nonetheless, the decrease in tangent loss value is observed with that frequency ascribed in the sample to general dielectric phenomenon such that polarization at lower frequency and vice versa. For sample CSONT 2, tangent loss initially decreases to 80°C and is constant to 225°C and then increases. Furthermore, for doped CSONT 2 sample, the value of tangent loss is found to be lower than CSONT 0, which reconfirms the polarization of charge carrier become lower. Further, the conduction mechanism is also explored in the following section.

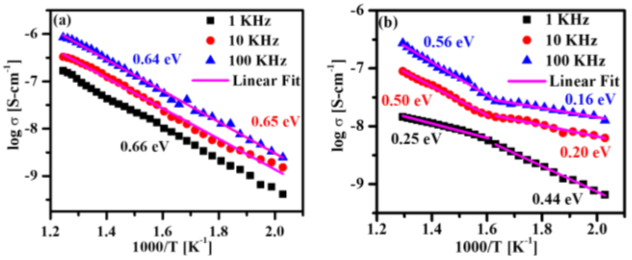

Fig. 8. Variation of logarithmic conductivity with respect to inverse of temperature at three different frequencies, 1 KHz, 10 KHz and 100 KHz **(a)** CSONT 0 **(b)** CSONT 2.

In addition, the ac conductivity of samples was studied as a function of temperature at three different frequencies (1 KHz, 10 KHz and 100 KHz) for samples CSONT 0 and CSONT 2. **Fig. 8** show the Arrhenius plot for pure and doped samples at three frequencies. The CSONT 0 sample reveals a single conduction region at all frequencies. It is also found from thermal dependence of conductivity; it does not converge into a single region that represents conduction occurred between the delocalized states of Sn in CSONT 0 and Sn/Ti in CSONT 2 sample. The value of conductivity for both the samples was increased with that temperature, showing the semiconducting nature of samples, which is well agreement with UV-Vis. absorbance study. The ac-conductivity was analyzed using Arrhenius model to explore the conduction mechanism. According to Arrhenius model, the conductivity is related with temperature by following equation [**41**];

$$\sigma = \sigma_o \exp\left(-\frac{E_{cond.}}{k_B T}\right)$$

Taking log on both sides, it gives

$$\log\sigma = \log\sigma_o + \left(-\frac{E_{cond.}}{1000 * k_B} * \frac{1000}{T}\right) \tag{12}$$

The Arrhenius plot for both samples was generated using equation (12) for both sample and fitted to experimental data. The terms $\log\sigma_o, k_B, E_{cond.}$ are pre-exponential factor, Boltzmann constant, activation energy required to conduct the charge carrier respectively. The activation energy was found to be 0.66 eV, 0.65 eV, and 0.64 eV at frequency 1 KHz, 10 KHz, and 100 KHz respectively for sample CSONT 0. It is further noted that the activation energy decreases with that frequency, which may be due to lower time needed to hop the charge carrier between delocalized sites. The value of activation energy approx. 1 eV for perovskite oxides, assigned to the migration of oxygen vacancies while less than 0.5 eV assigned to pure electronic conduction and in between these values is assigned to the mixed ionic and electronic conductors [**49,53,54**]. Based on the values of activation energy, conduction is indicated by following two mechanisms;

(i) Due to long range migration of charge carrier between the degenerate sites of Sn.
(ii) Due to conduction of electron between degenerate sites of Sn as well as migration of oxygen vacancy to the neighbour vacant oxygen sites.

Because the conductivity depends not only on charge carrier concentration but also on drift velocity of charge carrier.

Moreover, the ac conductivity of doped sample indicates two forms of conduction region are operative in CSONT 2, and the activation energy value is 0.44 eV, 0.20 eV, and 0.16 eV in the low temperature region and 0.25 eV, 0.50 eV, 0.56 eV at frequency 1 KHz, 10 KHz, and 100 KHz respectively. The value of the activation energy obtained in low temperature region is assigned to the conduction of electron between Sn^{4+} and Ti^{4+}, whereas the higher value of the activation energy is ascribed to the mixed ionic and electronic conduction (electron between Sn^{4+} to Sn^{2+} site, and oxygen vacancy to nearest vacant sites of oxygen). It is further found that the conductivity decreases with incorporation of Nd. To explain this variation, the charge compensation mechanism was taken into account as given by equation (9). There are two mechanisms proposed in Dielectric study. When charge compensation mechanism takes place by second path, the conductivity increases while according to first path the conductivity should be decreased. Therefore, based on this analysis, we infer that the charge compensation mechanism takes place by creation of cationic vacancy that is heavier than electron and oxygen ion, resulting in reduced conductivity.

Based on the value of dielectric constant, tangent loss, activation energy and optical properties, the present materials can be used as thermally stable capacitor, mixed ionic electronic conductor, UV-filter, UV-sensor and semiconductor devices application.

Conclusions

The single phase of pure and doped (Nd at Ca-site, Ti at Sn-site) $CaSnO_3$ was successfully synthesized using sol-gel method followed by 800ºC calcination and 900ºC sintering. The shift in XRD peak to higher angle suggests the incorporation of Nd at Ca-site, and Ti at Sn-site, due to lower ionic radii of dopants than host, which further results in compression of unit cell. Furthermore, the Rietveld refinement analysis indicates that the samples were crystallized into orthorhombic crystal structure similar to undoped. The UV Vis. studies of samples show minimum reflectance in UV and higher in visible to NIR range, making it suitable for UV-filter and sensor application. The optical band gap is further narrowed by incorporation of Nd and Ti in $CaSnO_3$. The dielectric constant of both samples (30 and 18) was found to be temperature independent up to 220ºC and 300ºC and tangent loss below 1 makes it suitable candidate for thermally stable capacitor application. Nonetheless, the activation energy of pure $CaSnO_3$ sample reflects electronic conduction between degenerate's sites of Sn^{4+}/Sn^{2+} while mixed ionic and electronic conducting (MIECs) for Nd and Ti-doped $CaSnO_3$ sample. Based on the activation energy value, the present material can be used as MIECs applications.

Acknowledgement

AK thankfully acknowledges the University Grant Commission (UGC) of India for providing UGC research fellowship. We wish to thank Department of Science and Technology (DST), Government of India, New Delhi for financial support under FIST grant.

Keywords

Perovskite $CaSnO_3$; rietveld refinement, reflectance spectroscopy, dielectric properties, arrhenius conduction.

Received: 29 May 2020
Revised: 11 June 2020
Accepted: 01 September 2020

References

1. Megaw, H. D.; *Proc. R. Soc. London. Ser. A. Math. Phys. Sci.*, **1947**, *189*, 261.
2. Maul, J.; Erba, A.; Santos, I. M. G.; Sambrano, J. R.; Dovesi, R.; *J. Chem. Phys.*, **2015**, *142*, 014505.
3. Yangthaisong, A.; *Chinese Phys. Lett.*, **2013**, *30*, 077101.
4. Singh, M. K.; Karan, N. K.; Katiyar, R. S.; Scott, J. F.; Jang, H. M.; *J. Phys. Condens. Matter* **2008**, *20*, 055210.
5. Singh, M. K.; Hong, J. W.; Karan, N. K.; Jang, H. M.; Katiyar, R. S.; Redfern, S. A. T.; Scott, J. F.; *J. Phys. Condens. Matter* **2010**, *22*, 095901.
6. Muralidharan, M.; Anbarasu, V.; Elaya Perumal, A.; Sivakumar, K.; *J. Mater. Sci. Mater. Electron.* **2017**, *28*, 4125.
7. Kumar, U.; Upadhyay, S.; *J. Mater. Sci. Mater. Electron.* **2020**, *31*, 5721.
8. Kumar, U.; Ansaree, J.; Upadhyay, S.; *Process. Appl. Ceram.* **2017**, *11*, 177.
9. Azad, A. M.; Shyan, L. L. W.; Alim, M. A.; *J. Mater. Sci.* **1999**, *34*, 3375.
10. Azad, A. M.; Shyan, L. L. W.; Alim, M. A.; *J. Mater. Sci.* **1999**, *34*, 1175.
11. Stanulis, A.; Sakirzanovas, S.; Van Bael, M.; Kareiva, A.; *J. Sol-Gel Sci. Technol.* **2012**, *64*, 643.
12. Chen, X. Y.; Ma, C.; Bao, S. P.; Zhang, H. Y.; *J. Alloys Compd.* **2010**, *497*, 354.
13. Shi, M.; Zhao, H.; Zou, J.; Yang, B. B.; Li, Y.; Wang, Z.; Chang, C.; Li, W.; *J. Mater. Sci. Mater. Electron.* **2017**, *28*, 10067.
14. Sharma, N.; Shaju, K. M.; Rao, G. V. S.; Chowdari, B. V. R.; *J. Power Sources* **2005**, *139*, 250.
15. Zhang, B.; Shi, M.; Zhang, D.; Guo, Y.; Chang, C.; Song, W. J.; *J. Mater. Sci. Mater. Electron.* **2017**, *28*, 11624.
16. Cheng, H.; Lu, Z.; *Solid State Sci.* **2008**, *10*, 1042.
17. Lucena, G. L.; De Lima, L. C.; Honório, L. M. C.; De Oliveira, A. L. M.; Tranquilim, R. L.; Longo, E.; De Souza, A. G.; A. Da S

Maia, I. M. G. dos Santos, *Ceramica* **2017**, *63*, 536.
18. Pang, T.; Lu, W.; Shen, W.; *Phys. B Condens. Matter* **2016**, *502*, 11.
19. Lu, Z.; Liu, J.; Tang, Y.; Li, Y.; *Inorg. Chem. Commun.* **2004**, *7*, 731.
20. Alves, M. C. F.; Souza, S. C.; Lima, S. J. G.; Longo, E.; Souza, A. G.; Santos, I. M. G.; *J. Therm. Anal. Calorim.* **2007**, *87*, 763.
21. A. West, *Solid State Chemistry and Its Applications, 2nd Edition, Student Edition*, **2014**.
22. Stoumpos, C. C.; Malliakas, C. D.; Kanatzidis, M. G.; *Inorg. Chem.* **2013**, *52*, 9019.
23. Asim, N.; Ahmadi, S.; Alghoul, M. A.; Hammadi, F. Y.; Saeedfar, K.; Sopian, K.; *Int. J. Photoenergy* **2014**, 2014.
24. Bader, N.; Benkhayal, A. A.; Zimmermann, B.; *Int. J. Chem. Sci.* **2014**, *12*, 519.
25. Zhang, N.; Zhang, Z. C.; Zhou, J. G.; *J. Sol-Gel Sci. Technol.* **2011**, *58*, 355.
26. Dohnalová, Ž.; Šulcová, P.; Trojan, M.; *J. Therm. Anal. Calorim.* **2008**, *93*, 857.
27. Liang, Z.; Zhang, J.; Sun, J.; Li, X.; Cheng, L.; Zhong, H.; Fu, S.; Tian, Y.; Chen, B.; *Phys. B Condens. Matter* **2013**, *412*, 36.
28. Saha, S.; Das, S.; Ghorai, U. K.; Mazumder, N.; Ganguly, D.; Chattopadhyay, K. K.; *J. Phys. Chem. C* **2015**, *119*, 16824.
29. Fan, C.; Song, X.; Yu, H.; Yin, Z.; Xu, H.; Cao, G.; Zheng, D.; Sun, S.; *Mater. Lett.* **2007**, *61*, 1588.
30. Tsega, M.; Dejene, F. B.; *Bull. Mater. Sci.* **2017**, *40*, 1347.
31. Sumithra, S.; Jaya, N. V.; *J. Mater. Sci. Mater. Electron.* **2018**, *29*, 4048.
32. Sumithra; Victor Jaya, N.; *Mater. Res. Innov.* **2019**, *23*, 375.
33. Shein, I. R.; Kozhevnikov, V. L.; Ivanovskii, A. L.; *Semiconductors* **2006**, *40*, 1261.
34. Goethals, J.; Fourdrin, C.; Tarrida, M.; Bedidi, A.; Hatert, F.; Rossano, S.; *Phys. Chem. Miner.* **2019**, *46*, 143.
35. Kurre, R.; Bajpai, P. K.; *AIP Conf. Proc.* **2011**, *1372*, 198.
36. Singh, S.; Singh, P.; Parkash, O.; Kumar, D.; Singh, S.; Singh, P.; Parkash, O.; Kumar, D.; *Adv. Appl. Ceram.* **2017**, *106*, 231.
37. Callister, W. D.; *Mater. Des.* **2003**, DOI 10.1016/0261-3069(91)90101-9.
38. De Souza, S. C.; Alves, M. C. F.; De Oliveira, A. L. M.; Longo, E.; Ticiano Gomes Vieira, F.; Gomes, R. M.; Soledade, L. E. B.; De Souza, A. G.; Garcia Dos Santos, I. M.; *J. Therm. Anal. Calorim.* **2009**, *97*, 185.
39. Shannon, R. D.; Prewitt, C. T.; *Acta Crystallogr. Sect. B Struct. Crystallogr. Cryst. Chem.* **1970**, *26*, 1046.
40. Kumar, U.; Ansaree, M. J.; Verma, A. K.; Upadhyay, S.; Gupta, G.; *Mater. Res. Express* **2017**, *4*, 116304.
41. Kumar, U.; Ankur, K.; Yadav, D.; Upadhyay, S.; *Mater. Charact.* **2020**, *162*, 110198.
42. Kumar, A.; Khan, B.; Dixit, A.; Kumar, U.; *J. Mater. Sci. Mater. Electron.* **2020**, 1.
43. Prabhu, Y. T.; Rao, K. V.; *World J. Nano Sci. Eng.* **2014**, *2014*, 21.
44. Kumar, U.; Yadav, D.; Thakur, A. K.; Srivastav, K. K.; Upadhyay, S.; *J. Therm. Anal. Calorim.* **2018**, *135*, 1987.
45. Kumar U, U. S.; Yadav D.; *J. Am. Ceram. Soc.* **2020**, *00*, 1.
46. Zhang, Y.; Zhang, H.; Wang, Y.; Zhang, W. F.; *J. Phys. Chem. C* **2008**, *112*, 8553.
47. Kumar, U.; Upadhyay, S.; *Mater. Res. Express* **2019**, *6*, 055805.
48. Kumar, U.; Upadhyay, S.; *Mater. Lett.* **2018**, *227*, 100.
49. Lenin, N.; Sakthipandi, K.; Kanna, R. R.; Rajesh, J.; *Ceram. Int.* **2018**, *44*, 11562.
50. Alahmari, F.; Almessiere, M. A.; Ünal, B.; Slimani, Y.; Baykal, A.; *Ceram. Int.* **2020**, *4*, DOI 10.1016/j.ceramint.2020.06.249.
51. Ünal, B.; Almessiere, M. A.; Korkmaz, A. D.; Slimani, Y.; Baykal, A.; *J. Rare Earths* **2020**, *In Press*, DOI 10.1016/j.jre.2019.09.011.
52. Almessiere, M. A.; Ünal, B.; Slimani, Y.; Korkmaz, A. D.; Baykal, A.; Ercan, I.; *Results Phys.* **2019**, *15*, 102755.
53. Yang, X.; Liu, S.; Lu, F.; Xu, J.; Kuang, X.; *J. Phys. Chem. C* **2016**, *120*, 6416.
54. Almessiere, M. A.; Unal, B.; Baykal, A.; *J. Rare Earths* **2018**, *36*, 1310.